

# Faster Determination of Mass-Averaged SAR From 2-D Area Scans

Michael Y. Kanda, *Member, IEEE*, Mark G. Douglas, *Member, IEEE*, Edwin D. Mendivil, Maurice Ballen, Andrew V. Gessner, and Chung-Kwang Chou, *Fellow, IEEE*

**Abstract**—An algorithm is presented that accurately and quickly estimates the peak 1- or 10-g averaged specific absorption rate (SAR) in a human phantom when exposed to a wireless device. Instead of performing both an area scan and a zoom scan (as per international standards), only the area scan and knowledge of the transmit frequency are needed. The accuracy of the algorithm has been demonstrated across a broad frequency range (150–2450 MHz) and for both 1- and 10-g averaged SAR using a sample of 264 SAR measurements from 55 wireless handsets. For the sample size studied, the root-mean-squared errors of the algorithm are 1.2% and 5.8% for 1- and 10-g averaged SAR, respectively. It is shown that the algorithm works well in both head and body phantoms.

**Index Terms**—Dosimetry, mobile phones, specific absorption rate (SAR), wireless.

## I. INTRODUCTION

SPECIFIC absorption rate (SAR) is a metric that quantifies the exposure of a person to RF energy from wireless transmitters [1], [2]. Some national regulatory agencies limit RF exposure and require that the peak mass-averaged SAR (averaged over a 1- or 10-g mass of tissue) due to a wireless transmitter is evaluated in order to demonstrate compliance with their rules prior to equipment authorization or use (e.g., [3]). To measure SAR from a wireless handset, the handset is placed against a human-shaped phantom and the electric field is scanned inside the phantom [4], which is filled with a liquid whose dielectric properties approximate those of living tissue (see Fig. 1).

The measurement of SAR from wireless handsets has recently been standardized [5], [6]. An initial coarse two-dimensional (2-D) scan (area scan) is performed in the phantom liquid on a surface at a fixed distance  $z_d$  away from the phantom surface. The area scan covers the projection of the handset (see Fig. 2). From the area scan, the location of maximum SAR is found. At this location, a higher resolution three-dimensional (3-D) scan (zoom scan) is performed, and post-processing is used to determine the peak mass-averaged SAR. Scanning of the electric field is performed by moving an electric-field probe throughout the liquid with the aid of a robot or similar positioning equipment. This scanning is time consuming. The time spent to perform one complete measurement (area and

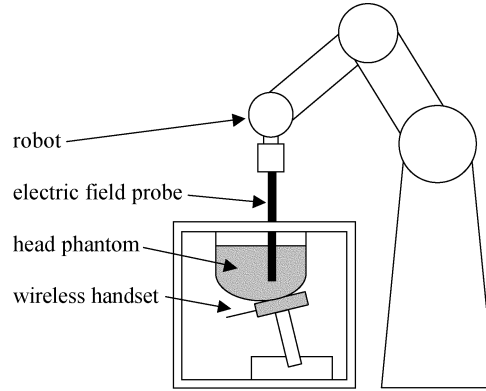


Fig. 1. Typical SAR measurement system. The wireless handset is held next to the ear of the liquid-filled head phantom, which is laying on its side.

zoom scan) is typically on the order of half an hour,<sup>1</sup> and over 100 measurements may be needed for full SAR compliance evaluation, given the combinations of transmit frequency bands and modes, device positions against the body and left- and right-hand sides of head phantoms, handset configurations (e.g., extended and retracted antennas), accessories, etc. Therefore, a faster means of estimating the peak mass-averaged SAR is very desirable.

The use of 2-D area scans to estimate the peak mass-averaged SAR was proposed by Manning and Massey [7]. They established that a correlation exists between the highest measured SAR in the area scan and the peak mass-averaged SAR. The correlation was analyzed using cellular telephone handsets at two frequencies (900 and 1800 MHz).<sup>2</sup>

In a similar proposal [8], the SAR distribution is reconstructed from approximately 30 measurement points assuming that the SAR has an ellipsoidal distribution. The measurement grid consists of a  $4 \times 4$  point area scan and additional points in the  $z$ -direction. SAR data are fitted to the ellipsoidal model using an iterative procedure. The method was validated using cellular telephone handsets at 900 and 1800 MHz.

This paper proposes a robust algorithm for estimating the peak mass-averaged SAR from a 2-D area scan [9], [10]. The algorithm requires only the measurement of the area scan and

<sup>1</sup>Actual measurement time depends on the number of measurement points in the area and zoom scans, the measurement time at each point, and the time taken to move between points. Measurement times on the order of half an hour are typical at Motorola using a DASY3 measurement system from Schmid & Partner Engineering AG, Zürich, Switzerland, in a manner consistent with international standards [5], [6].

<sup>2</sup>M. Manning, “Principles on which the 2D scanning system is based,” IndexSAR website. [Online]. Available: <http://www.indexsar.com/2dprinciples.htm>, 2003.

Manuscript received November 21, 2003; revised January 28, 2004.

The authors are with the Corporate Electromagnetic Energy Research Laboratory, Motorola Laboratories, Fort Lauderdale, FL 33322 USA.

Digital Object Identifier 10.1109/TMTT.2004.832026

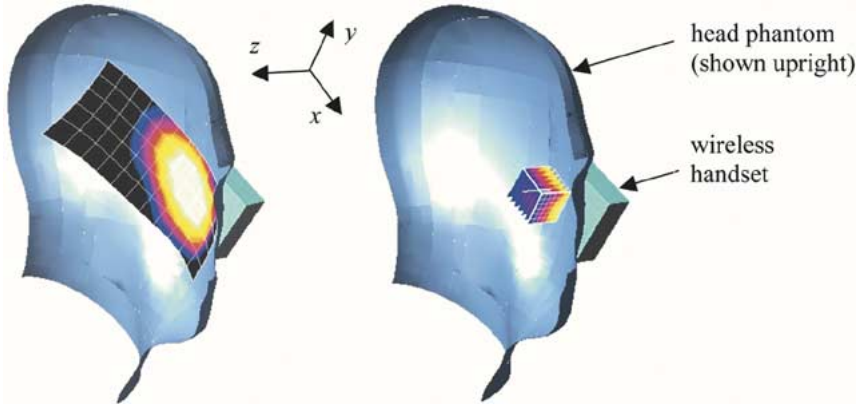


Fig. 2. Examples of: (left) an area scan and (right) a zoom scan of a wireless handset in a human-shaped phantom. By convention, the surface of the area scan conformal to the phantom boundary is called the  $x$ - $y$ -plane, and the direction away from the phantom boundary and into the phantom is the  $z$ -direction. This figure was generated using DASY4 software from Schmid & Partner Engineering AG. Color scales are relative, with white representing the highest SAR and black representing the lowest SAR.

knowledge of the transmit frequency. The accuracy of the algorithm has been demonstrated across a broad frequency range (150–2450 MHz) and for both 1- and 10-g averaged SAR using a sample of 264 SAR measurements of 55 wireless handsets. The proposed algorithm will be shown to be more robust than the method of [7], as it estimates the mass-averaged SAR from an averaged value over a footprint of the area scan instead of the peak value. Unlike the method of [8], the proposed algorithm does not require measurements in the  $z$ -direction, and it does not rely on assumptions of the field distribution in the  $x$ - $y$ -plane. Therefore, it applies equally to SAR distributions that are strongly asymmetric (e.g., distributions containing multiple peaks). The algorithm does not need to know the phantom or tissue types (head or body, as defined in [5] and [6]).

## II. METHODOLOGY

To find the peak mass-averaged SAR from the zoom scan, the data are extrapolated and interpolated onto a fine grid (e.g., 1-mm resolution) and averaged over all volumes  $V$  containing the 1- or 10-g mass in the shape of a cube (with tolerances as specified in [5] and [6]). The peak mass-averaged SAR ( $SAR_v$ ) is then the highest of these averaged SAR values, defined over the volume  $V_{\max}$

$$SAR_v = \frac{1}{V} \iiint_{V_{\max}} SAR(x, y, z) dx dy dz. \quad (1)$$

To estimate  $SAR_v$  using less data, assumptions must be made about the field distributions. The distribution of SAR in the  $x$ - $y$ -plane is, in general, complex. In many cases, the contours of the distribution have an ellipsoidal shape [8], but in some cases, the distribution is strongly asymmetric and may contain multiple peaks. On the other hand, it is well known that the SAR distribution in the  $z$ -direction has a simple exponential decay for a variety of homogeneous phantoms [11], [12]

$$SAR(z) = SAR(0) e^{-\frac{2z}{\delta}} \quad (2)$$

where  $\delta$  is the penetration depth determined from the measured data. If the SAR is only known at a distance  $z = z_d$  from the phantom surface, then (2) becomes

$$SAR(z) = SAR(z_d) e^{-\frac{2(z-z_d)}{\delta}} = SAR(z_d) S(z, z_d) \quad (3)$$

where  $\hat{\delta}$  is an estimate of the penetration depth (the true penetration depth is unknown) and  $S(z, z_d)$  is a unitless decay characteristic. An assumption must also be made about the dependence of the  $x$ - $y$  distribution on the  $z$ -distribution. For this model, it is assumed that they are independent, i.e.,

$$SAR(x, y, z) = SAR(x, y, z_d) S(z, z_d) \quad (4)$$

where  $SAR(x, y, z_d)$  is the SAR in the  $x$ - $y$ -plane measured at a distance  $z = z_d$  from the phantom surface. This assumption is not strictly true. The direction of field propagation is nearly (but not exactly) parallel to the  $z$ -direction. Therefore, the local peak SAR migrates in  $x$  and  $y$  as it propagates. Also, the field spreads in the  $x$ - and  $y$ -directions as it propagates, given that the wavefront is somewhat spherical. However, these effects are not very pronounced and, as will be seen, the assumption is a good one.

Substituting (3) and (4) into (1) gives  $SAR_e$ , which is an estimate of  $SAR_v$

$$SAR_e = \frac{1}{V} \iiint_{V_{\max}} SAR(x, y, z_d) S(z, z_d) dx dy dz \quad (5)$$

$$= \frac{1}{L_c^2} \iint_{A_{\max}} SAR(x, y, z_d) dx dy \times \frac{1}{L_c} \int_0^{L_c} e^{-\frac{2(z-z_d)}{\delta}} dz \quad (6)$$

$$= \frac{1}{L_c^2} \iint_{A_{\max}} SAR(x, y, z_d) dx dy \frac{\hat{\delta}}{2L_c} e^{\frac{2z_d}{\delta}} \left( 1 - e^{-\frac{2L_c}{\delta}} \right) \quad (7)$$

where  $L_c = V^{1/3}$  is the side length of the 1- or 10-g cube ( $L_c = 10$  mm or 21.5 mm, respectively, for a tissue density of 1 g/cm<sup>3</sup>). The first integral of (6) is the highest footprint-averaged SAR. This is determined by averaging the area scan over all square

areas  $A = L_c^2$  (the footprint of the 1- or 10-g cube) and finding the highest of these, defined over the area  $A = A_{\max}$ .

The proposed algorithm is as follows:

- conduct an area scan with measurement resolution  $\Delta x$ ,  $\Delta y$ ;
- use cubic spline interpolation to determine  $SAR(x, y)$  over a 1-mm resolution;
- search for the highest 1- or 10-g footprint of  $SAR(x, y, z_d)$ ;
- find  $SAR_e$  from (7) using the trapezoidal rule for integration.

The only unknown in (7) is the estimate of the penetration depth  $\hat{\delta}$ . This is a frequency-dependent variable that will be determined in Section IV-A.

### III. ANALYTICAL EVALUATION

The accuracy of the algorithm depends largely on the accuracy of the interpolation of the area scan, which, in turn, depends on the area-scan resolution. The area scan uses a coarse measurement resolution (typically  $\Delta x = \Delta y = 10$  mm or 15 mm). To quantify the interpolation errors, three analytical reference functions were sampled at a 15-mm resolution and interpolated onto a 1-mm resolution. These three functions are defined in international SAR measurement standards (e.g., [5]) to represent a range of SAR distributions in the 300–3000-MHz frequency range

$$f_1(x, y, z) = e^{\frac{-z}{2a}} \cos^2 \left( \frac{\pi}{2} \frac{\sqrt{x'^2 + y'^2}}{5a} \right) \quad (8)$$

$$f_2(x, y, z) = e^{\frac{-z}{a}} \frac{a^2}{a^2 + x'^2} \left( 3 - e^{\frac{-2z}{a}} \right) \cos^2 \left( \frac{\pi}{2} \frac{y'}{3a} \right) \quad (9)$$

$$f_3(x, y, z) = \frac{a^2}{\frac{a^2}{4} + x'^2 + y'^2} \left( e^{\frac{-2z}{a}} + \frac{a^2}{2(a + 2z)^2} \right) \quad (10)$$

where  $x' = x + d$ ,  $y' = y + d$ , and  $a = 20$  mm. Varying  $d$  over the range 0 to  $\Delta x$  shifts the measurement grid so that it is not aligned with the peak ( $d = 0$  gives perfect alignment of the grid with the peak,  $d = \Delta x/2$  gives the worst case shift). These functions were sampled at  $z = 4.7$  mm (a typical probe distance for the area scan). The impact of alignment of the sampling grid on interpolation is shown in Fig. 3 for function  $f_3$  using a shift of  $d = \Delta x/2$ . Function  $f_3$  has the steepest spatial variation and was designed to give the worst case interpolation errors.

To determine the accuracy of interpolation, the percent error of the peak sampled SAR, the peak interpolated SAR, and the average over the highest 1- and 10-g SAR footprint were found. These values are plotted in Fig. 4 as a function of  $d$  for function  $f_3$ . The average errors are shown in Table I.

The errors for functions  $f_1$  and  $f_2$  are small, but for  $f_3$ , the errors are considerable. These errors can be significantly improved by using a finer 10-mm area-scan resolution (bottom line of Table I). The high field gradients characterized by  $f_3$  are typically considerably sharper than seen in the experimental data. The averaging of the SAR over the mass footprint gives the lowest errors, as expected, which justifies its use in the algorithm.

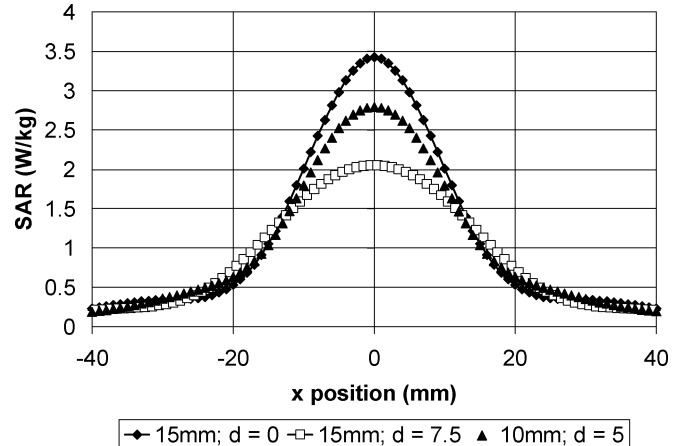


Fig. 3. Peak profiles of function  $f_3$  are shown for perfect alignment ( $d = 0$ ) and worst case alignment ( $d = \Delta x/2$  for resolutions of  $\Delta x = 15$  mm and 10 mm). The results presented are interpolated to a 1-mm resolution.

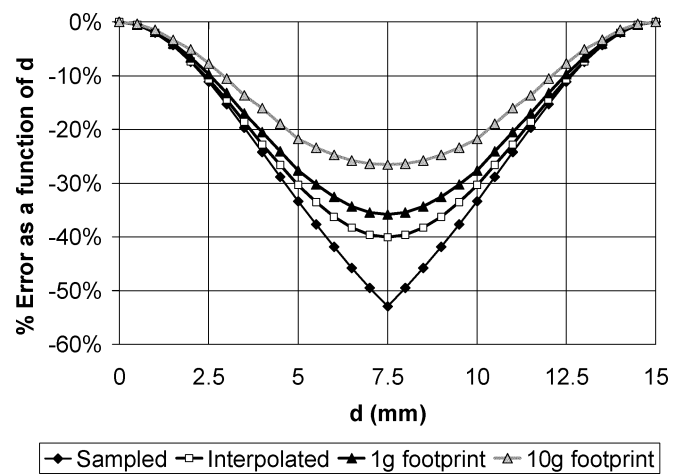


Fig. 4. Percent errors in the peak value (sampled and interpolated peaks) and average value (over the highest 1- and 10-g footprint) versus shift distance  $d$  for function  $f_3$  with  $\Delta x = \Delta y = 15$  mm.

TABLE I  
AVERAGE OF THE PERCENT ERRORS IN THE PEAK AND AVERAGE SAR VALUES

Function	$\Delta x, \Delta y$	Peak, measured	Peak, interpolated	Average, 1g footprint	Average, 10g footprint
$f_1$	15 mm	-0.9%	-0.1%	0.0%	0.0%
$f_2$	15 mm	-5.3%	-3.2%	-2.5%	-1.0%
$f_3$	15 mm	-22.4%	-19.7%	-17.8%	-13.7%
$f_3$	10 mm	-12.4%	-8.7%	-5.9%	-2.0%

### IV. EXPERIMENTAL EVALUATION

To test the accuracy of the algorithm experimentally, SAR measurement data were collected on a variety of wireless handsets. A total of 264 data files from 55 different handsets were collected, with transmit frequencies ranging from 150 to 2450 MHz (see Table II). The 55 handsets use a variety of signaling schemes [e.g., analog, NADC, global system for mobile communication (GSM), code division multiple access (CDMA)]. There are a total of 146 measurements against the head and 118 against the body. Efforts were made to select measurement data in a wide variety of test configurations (e.g., cheek versus tilt position and left- versus right-hand side for

TABLE II  
NUMBER OF SAR DATA FILES AND PRODUCTS PER FREQUENCY INCLUDED  
IN THE EXPERIMENTAL EVALUATION. SOME PRODUCTS OPERATE AT  
MULTIPLE FREQUENCIES

$f$ (MHz)	Data files	Products
150	32	7
230	15	1
450	34	13
835	59	12
900	32	13
1750	39	15
1880	43	12
2450	10	3
Total	264	55

head data, different carry accessories for body-worn data) and a wide range of SAR values (from 0.4 to 8 W/kg for the 1-g averaged SAR). The SAR distributions in the  $x$ - $y$ -plane also vary widely from symmetric single-peak distributions to asymmetric distributions with multiple peaks (Fig. 5).

Each data file includes both the area and zoom scans, measured using a DASY3 system from Schmid & Partner Engineering AG [13]. The area-scan resolution is  $\Delta x = \Delta y = 15$  mm for all data files. For the zoom scans, 80% of files (211) have seven points in all directions with resolution of  $\Delta x = \Delta y = \Delta z = 5$  mm. The remaining 53 files have five points in  $x$  and  $y$  with a resolution of  $\Delta x = \Delta y = 8$  mm and seven points in  $z$  with a resolution of  $\Delta z = 5$  mm.

The accuracy of the estimate  $SAR_e$  is determined by comparing it with  $SAR_v$  from (1).  $SAR_v$  is calculated from the zoom scan data after fourth-order extrapolation and cubic spline interpolation. Integration is performed using the trapezoidal rule. Since  $SAR_e$  is determined from the area scan and  $SAR_v$  is determined from the zoom scan, and because the output power of a handset may drift during the measurement,  $SAR_e$  was corrected for this drift.

#### A. Penetration Depth

An estimate of the penetration depth, i.e.,  $\hat{\delta}$ , must be determined in order to evaluate  $SAR_e$ . For the 264 data files, the penetration depth along the direction of the peak SAR was determined. The penetration depth is dependent on frequency and the dielectric parameters of the tissue-simulating liquid. For all of the data files, the dielectric parameters were within  $\pm 5\%$  of the target values in Table III. The target dielectric parameters of head-simulating liquid above 300 MHz were determined by Drossos *et al.* [14] for international standards (e.g., [5]). All of the targets for body-simulating liquid and the targets for head-simulating liquid below 300 MHz were determined by the U.S. Federal Communications Commission (FCC), Washington, DC, for its guidelines [15].

On average, the permittivity and conductivity are approximately 30% and 8% higher for body-simulating liquid than for head-simulating liquid. However, the impact of these differences partially cancel each other out, resulting in penetration depths that are not strongly dependent on the tissue type. This can be seen in Fig. 6 for the case of a plane wave at normal in-

cidence to a flat phantom, where the penetration depth is given by

$$\delta = \frac{1}{\omega \sqrt{\left(\frac{\mu_0 \epsilon_r \epsilon_0}{2}\right) \left(\sqrt{1 + \left(\frac{\sigma}{\omega \epsilon_r \epsilon_0}\right)^2} - 1\right)}}. \quad (11)$$

In Fig. 6, the difference in penetration depths between head and body tissue is only approximately 6% at most frequencies. For this reason, it makes sense to choose a penetration depth that is independent of tissue type.

The penetration depth is also dependent on the current distribution of the source [device-under-test (DUT)] and on the distance of the source to the phantom. The penetration depth in a flat phantom due to dipole antenna sources is shown in Fig. 6 for measurements in head-tissue simulating liquids. The distance from the feed point of the dipole antennas to the tissue simulating liquid was 15 mm for frequencies below 1 GHz and 10 mm otherwise (as specified in [5] and [6]). It can be seen in Fig. 6 that the penetration depth is smaller for a dipole antenna source than for a plane-wave source at the same frequency. The close proximity of the dipole antenna feed point means that the  $E$ -field in the tissue simulating liquid has a wavefront that is more spherical than planar, resulting in a faster decay of the SAR. Larger distances between the RF source and the phantom liquid result in larger penetration depths, as demonstrated in [11] and [12].

The average penetration depths from the 264 scans are shown in Fig. 6 as a function of frequency. As expected, the average values for head and body tissue simulating liquids (red squares and green diamonds, respectively) are very close to each other. The error bars represent a range of  $\bar{\delta} \pm 2s$ , where  $\bar{\delta}$  (blue circles) is the average of the head and body data and  $s$  is the sample standard deviation. It is noteworthy that the penetration depth values of the measured data are for the most part between the values for the plane wave and dipole antenna sources. This is because the cross-sectional area of the DUT source is larger than that of a dipole antenna (thus, the currents on the DUT will be more spread out) and the distance from the antenna feed point of the DUT to the phantom liquid is generally greater than that for the dipole antenna (due to the thickness of the DUT).

It can be seen from Fig. 6 that the average penetration depth is approximately linear with frequency. A least squares fit line through the average penetration depth values gives the following estimator  $\hat{\delta}$  of the penetration depth

$$\hat{\delta}[\text{mm}] = -10.7 f[\text{GHz}] + 40.4. \quad (12)$$

The estimator  $\hat{\delta}$  fits the average  $\bar{\delta}$  with a correlation coefficient of 98.8%, and the deviation of  $\hat{\delta}$  from  $\bar{\delta}$  is between 0.4%–6.2% across the 150–2450-MHz frequency range. This indicates that the least squares fit line is a good fit to the average data. Given that a large amount of data was used to derive this line, it is also expected to fit other data in an average sense. However, as indicated by the error bars in Fig. 6, the penetration depth can deviate significantly from one DUT to another at the same frequency. It is, therefore, important to analyze the sensitivity of  $SAR_e$  to the variation in the penetration

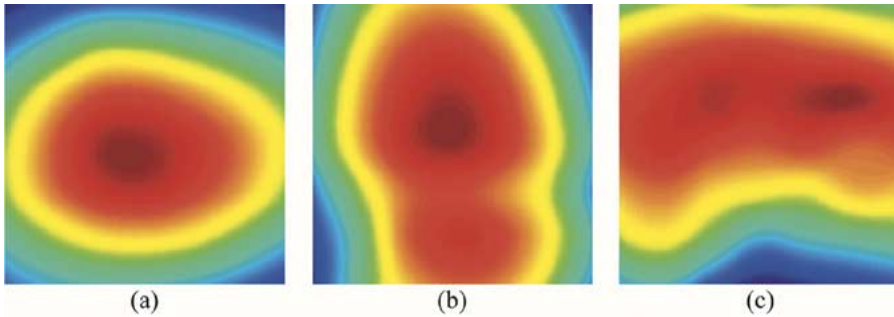


Fig. 5. SAR distributions in the  $x$ - $y$ -plane for three of the 264 data files. Although two of these SAR distributions are strongly asymmetric [(b) and (c)], the accuracy of  $SAR_e$  for each of the three examples is within 2% of the average errors overall (for both 1- and 10-g averaged SAR). Color scales are relative to each figure, with dark red representing the highest SAR and dark blue representing the lowest SAR.

TABLE III  
TARGET DIELECTRIC PARAMETERS OF THE PHANTOM LIQUID

$f$ (MHz)	Head [15, 16]		Body [15]	
	$\epsilon_r$	$\sigma$	$\epsilon_r$	$\sigma$
150	52.3	0.76	61.9	0.80
230	48.6	0.82	59.9	0.86
450	43.5	0.87	56.7	0.94
835	41.5	0.90	55.2	0.97
900	41.5	0.97	55.0	1.05
1750	40.0	1.37	53.4	1.49
1880	40.0	1.40	53.3	1.52
2450	39.2	1.80	52.7	1.95

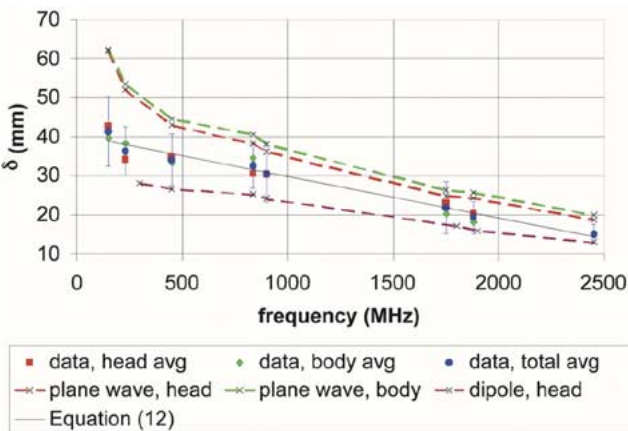


Fig. 6. Average penetration depth of the 264 data files compared with the penetration depths of the plane wave and dipole antenna sources.

depth. This was done by evaluating the second integral in (6) over a range of penetration depths (i.e., by calculating  $SAR_e$  while keeping the  $x$ - $y$  distribution constant). Fig. 7 shows the results for the range of penetration depths observed at 900 and 1750 MHz (the results are similar at other frequencies). The percent change in  $SAR_e$  at each value of  $\delta$  is shown relative to  $SAR_e$  at  $\delta = \hat{\delta}$ . Equation (12) gives a value of  $\hat{\delta} = 30.8$  mm and 21.7 mm at 900 and 1750 MHz, respectively. It can be seen that although the deviation of the penetration depth from  $\hat{\delta}$  is large (approximately  $\pm 25\%$ ), the deviation in  $SAR_e$  is within  $\pm 2\%$  and  $\pm 7\%$  for the 1- and 10-g averaged SAR, respectively. Also, the rms change in  $SAR_e$  for this data is 0.2% (1 g) and 2.8% (10 g) at 900 MHz, and 0.5% (1 g) and 3.2% (10 g) at 1750 MHz. These results show that the proposed method is relatively insensitive to differences between DUTs. The linear

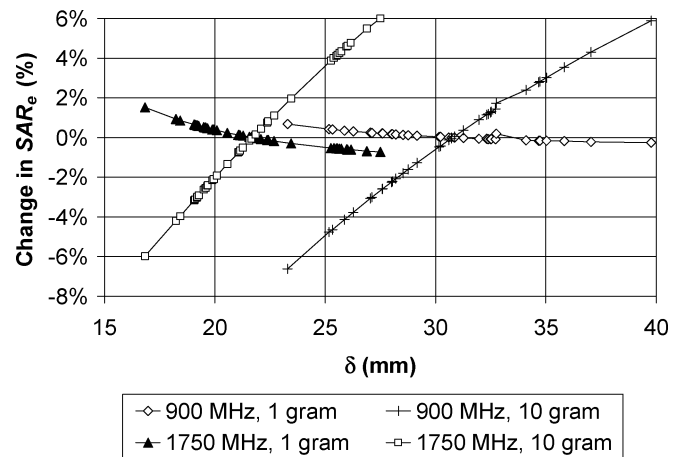


Fig. 7. Sensitivity of the  $SAR_e$  to the range of penetration depths observed at 900 and 1750 MHz for the data files considered in this study (32 and 39 data files, respectively; see Table II).

estimator  $\hat{\delta}$  of the penetration depth in (12) is, therefore, a good choice.

#### B. SAR Estimate

The area-scan estimate  $SAR_e$  of the peak 1- and 10-g averaged SAR (denoted  $SAR_{e,1g}$  and  $SAR_{e,10g}$ , respectively) were computed and compared with the volumetric SAR ( $SAR_{v,1g}$  and  $SAR_{v,10g}$ ) for all 264 scans. The linear correlation between  $SAR_e$  and  $SAR_v$  is excellent (Fig. 8). The correlation coefficient is 99.9% for both cases.

A histogram of the percent error of  $SAR_e$  relative to  $SAR_v$  is shown in Fig. 9, and the mean and rms errors at each frequency are given in Table IV. Note that the highest errors observed in the experimental data are much lower than the worst case errors observed from the analytical data. The rms error of the combined data is 1.2% and 5.8% for the 1- and 10-g averaged SAR, respectively. These errors are small compared to the estimated 12% uncertainty of our SAR measurement system (determined using the protocol in [5]). Treating the rms error of  $SAR_e$  and the uncertainty of the measurement system as independent random variables, their combined uncertainty is 12.1% and 13.3%, for the 1- and 10-g averaged SAR, respectively. Thus, the use of this area-scan SAR estimate in our SAR measurement system does not have a large impact on the total uncertainty.

Table IV shows that the smaller rms error of  $SAR_{e,1g}$  compared with  $SAR_{e,10g}$  is consistent across the frequency range.

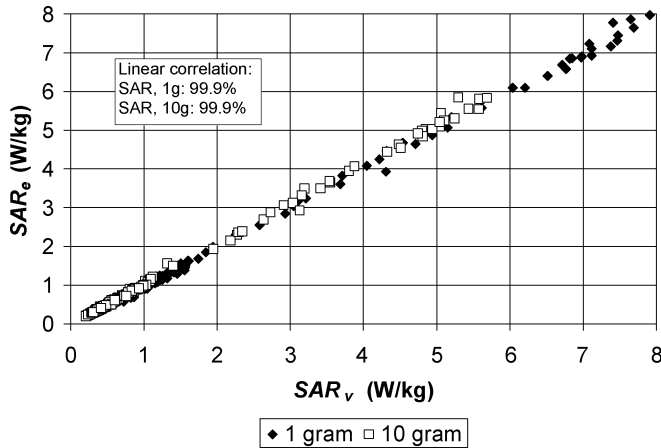


Fig. 8. Correlation between  $SAR_e$  and  $SAR_v$  for the 264 data files.

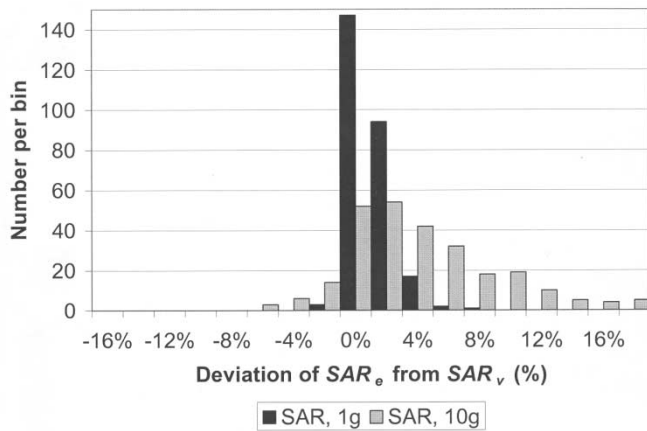


Fig. 9. Histogram of the deviation of  $SAR_e$  from  $SAR_v$  for the 264 data files. Data is grouped into bins of 2% increments along the  $x$ -axis. The  $y$ -axis shows the number of times the deviation fell within each bin.

TABLE IV  
MEAN AND rms ERRORS OF  $SAR_e$  RELATIVE TO  $SAR_v$ , FOR THE 264 DATA FILES. THE ERRORS ARE SHOWN BY FREQUENCY AND FOR ALL DATA COMBINED

$f$ (MHz)	$SAR_{e,1g}$		$SAR_{e,10g}$	
	Mean	RMS	Mean	RMS
150	-0.1%	0.8%	1.5%	5.0%
230	0.1%	0.9%	4.0%	4.7%
450	-0.6%	0.8%	2.4%	3.0%
835	-0.1%	0.9%	2.8%	5.2%
900	-0.4%	0.9%	2.3%	4.3%
1750	0.2%	1.1%	3.9%	7.5%
1880	0.8%	2.2%	5.6%	8.2%
2450	1.2%	1.6%	1.6%	3.4%
All data	<b>0.1%</b>	<b>1.2%</b>	<b>3.2%</b>	<b>5.8%</b>

It is evident from the previous discussion that this is due to the reduced sensitivity of  $SAR_{e,1g}$  to variations in the penetration depth from  $\hat{\delta}$  (from Fig. 7). This will be further explored in Section IV-C. The data in Table IV also shows that there are no strong frequency dependences of the rms error. From Fig. 9 and Table IV, it is also observed that  $SAR_e$  slightly overestimates  $SAR_v$ , giving a conservative estimate for these data.

RMS errors for head and body data may also be compared. For data taken with the head phantom, the rms errors are 1.4% and 6.3% for  $SAR_{e,1g}$  and  $SAR_{e,10g}$ , respectively. For data

taken with the body (flat) phantom, the rms errors are 1.0% and 5.0% for  $SAR_{e,1g}$  and  $SAR_{e,10g}$ , respectively. This shows that the algorithm works well regardless of phantom and tissue type. The slightly higher errors for the head phantom are expected, given that the complex shape of the head phantom results in higher measurement uncertainty.

### C. Algorithm Enhancements

From the analytical evaluation in Section III, it was demonstrated that the measurement resolution of the area scan can be a large source of error. From the analysis of penetration depths in Section IV-A, it was shown that the error in the assumption of the penetration depth can also be a source of error, particularly for  $SAR_{e,10g}$ . Clearly, the algorithm can be enhanced using a finer measurement resolution in  $x$  and  $y$  and/or additional measurements in  $z$  to give a better estimate of the penetration depth. However, this comes at the expense of longer measurement times. This section explores how the accuracy of the algorithm may be improved using these two enhancements.

Instead of assuming an exponential decay in  $z$  with an estimate of the penetration depth, SAR measurements along the  $z$ -direction can be used. For example, the SAR can be measured along one line in the  $z$ -direction (e.g., at the SAR peak in  $x$  and  $y$ ) after performing the area scan. The normalized average SAR along the  $z$ -direction is then used in place of the second integral in (6). This was done for the 264 data files using data from the zoom scan. The resulting rms errors are 1.9% for  $SAR_{e,1g}$  and 4.3% for  $SAR_{e,10g}$ . As expected, the use of the measured penetration depth has an impact on the rms error of  $SAR_{e,10g}$ , but has little impact on the rms error of  $SAR_{e,1g}$ . In fact, the rms error of  $SAR_{e,1g}$  increased slightly. This is explained by the fact that the measured penetration depth is on average smaller than  $\hat{\delta}$  (given that the direction of field propagation is not exactly parallel to the  $z$ -direction, the decay is sharper along  $z$  than along the direction of propagation). A smaller penetration depth results in a larger value of  $SAR_{e,1g}$  and a smaller value of  $SAR_{e,10g}$ , as shown in Fig. 7. From the histogram of Fig. 9, it can be seen how this will give a larger rms error for  $SAR_{e,1g}$  and a smaller rms error for  $SAR_{e,10g}$  for these data.

Thus far, the algorithm has been analyzed using coarse scan data with a resolution of  $\Delta x = \Delta y = 15$  mm. A finer measurement resolution of 5 mm was also analyzed. Since the existing area scans do not contain data at 5-mm resolution, this was accomplished by using the closest plane of the zoom scan data (the plane at  $z = z_d$ ). This data has either  $7 \times 7$  points with a 5-mm resolution (211 of 264 files) or  $5 \times 5$  points with an 8-mm resolution (53 files). To obtain a 5-mm resolution, the  $7 \times 7$  point grids were used (it was not possible to include the 8-mm resolution data for this case). Using the standard algorithm with this resolution gives rms errors of 0.9% and 2.8% for  $SAR_{e,1g}$  and  $SAR_{e,10g}$ , respectively.

If both enhancements are used together, the resulting rms errors are 0.6% and 0.9% for  $SAR_{e,1g}$  and  $SAR_{e,10g}$ , respectively. These errors are negligible and are comparable to the post-processing uncertainty of the zoom scan (due to interpolation, extrapolation, and averaging errors) [10]. In fact, from these results, it is questionable whether full measurement of the zoom scan is necessary. The coarse measurement resolution of the area

scan and the assumed SAR decay are the two largest sources of error of the algorithm. The errors due to other sources (e.g., post-processing, errors due to the dependence of the  $x$ - $y$  distribution on the  $z$ -distribution) are less than 1%.

## V. DISCUSSION

Given the robustness and accuracy of the algorithm, it can also be used for other purposes. For area scans having more than one SAR peak, international standards currently state that zoom scans should be performed on all secondary peaks whose peak SAR is within 2 dB of the primary peak [5], [6]. The algorithm could be used to estimate the peak mass-averaged SAR of the secondary peaks and determine whether measurement of the multiple zoom scans is really necessary.

The algorithm may also be used to evaluate the SAR of devices with simultaneous multifrequency transmission. An example of this is a cellular telephone that can simultaneously transmit a cellular telephone signal (e.g., at 900 MHz) and a Bluetooth signal (at 2450 MHz). It is possible that such a device may be compliant with the regulatory SAR limit at each frequency while the composite SAR from simultaneous transmission is above the limit. Therefore, the accurate determination of the SAR in this situation is important. As of this writing, this issue has not been standardized. Given that the tissue simulating liquid and the probe calibration are frequency dependent, and given that existing SAR measurement systems are unable to separate the frequency components of a signal, it is not possible to accurately measure the SAR from such a transmitter using one measurement in one liquid. It has been proposed instead that separate SAR measurements (area and zoom scans) are done at each frequency (using the appropriate tissue simulating liquid and probe calibration at that frequency) and the SAR distributions are added [16]. This method makes sense, but it may be very time consuming to implement, especially if the SAR peaks of the multiple transmitters are far apart due to the need to measure zoom scans that covers all peaks. A modification to this proposal is as follows.

- Step 1) Measure the area scan at each frequency.
- Step 2) Measure the SAR decay at the peak location of each area scan (*optional*).
- Step 3) For each area scan, numerically generate the volumetric SAR data, using either the measured decay (if Step 2) was performed) or an exponential decay with an estimate of the penetration depth. This step creates SAR data as if a zoom scan was performed covering the entire region of the area scan.
- Step 4) Add the resulting volumetric SAR distributions together.
- Step 5) Find the peak mass-averaged SAR.

This method has been proposed to international SAR measurement standard setting committees (IEEE SCC34 and IEC PT 62209). Aside from Step 4), this method is identical to the algorithm proposed in this paper. Therefore, the results shown in this paper are applicable to this procedure.

## VI. CONCLUSIONS

An algorithm has been presented that accurately and more quickly estimates the peak 1- or 10-g averaged SAR in a human phantom from a wireless device. Instead of performing both an area scan and a zoom scan, only the area scan and knowledge of the transmit frequency are needed. The accuracy of the algorithm has been demonstrated across a broad frequency range (150–2450 MHz) and for both 1- and 10-g averaged SAR using a sample of 264 SAR measurements from 55 wireless handsets. For the sample size studied, the root-mean-squared errors of the algorithm are 1.2% and 5.8% for 1- and 10-g averaged SAR, respectively. These errors are small compared to the total SAR measurement uncertainty.

## REFERENCES

- [1] *IEEE Standard for Safety Levels With Respect to Human Exposure to Radio Frequency Electromagnetic Fields, 3 kHz to 300 GHz*, IEEE Standard C95.1-1999, 1999.
- [2] ICNIRP, “International commission on nonionizing radiation protection guidelines for limiting exposure to time-varying electric, magnetic and electromagnetic fields (up to 300 GHz),” *Health Phys.*, vol. 74, no. 4, pp. 494–522, 1998.
- [3] “Evaluating compliance with FCC guidelines for human exposure to radiofrequency electromagnetic fields,” FCC, Washington, DC, FCC OET Bull. 65 Ed. 97-01, Aug. 1997.
- [4] Q. Balzano, O. Garay, and T. J. Manning, “Electromagnetic energy exposure of simulated users of portable cellular telephones,” *IEEE Trans. Veh. Technol.*, vol. 44, pp. 390–403, Aug. 1995.
- [5] *IEEE Recommended Practice for Determining the Peak Spatial-Average Specific Absorption Rate (SAR) in the Human Head From Wireless Communications Devices: Measurement Techniques*, IEEE Standard 1528-2003, 2003.
- [6] *Basic Standard for the Measurement of Specific Absorption Rate Related to Human Exposure to Electromagnetic Fields From Mobile Phones (300 MHz–3 GHz)*, CENELEC EN 50361 : 2001, 2001.
- [7] M. Manning and P. Massey, “Rapid SAR testing of mobile phone prototype using a spherical test geometry,” in *IEE Tech. on Antenna Measurements and SAR Seminar*, Loughborough, U.K., May 28–29, 2002.
- [8] J. C. Bolomey, “Efficient near-field techniques for human exposure evaluation: Applications to mobile and fixed antennas,” presented at the *Electromagnetic Environment and Human Exposure Evaluation Workshop of EMC*, Sorrento, Italy, 2002.
- [9] M. Y. Kanda, M. Ballen, M. G. Douglas, A. Gessner, and C.-K. Chou, “Fast SAR determination of gram-averaged SAR from 2-D coarse scans,” in *25th Annu. Bioelectromagnetics Society Meeting*, Wailea Maui, HI, June 2003, pp. 45–46.
- [10] M. G. Douglas, M. Y. Kanda, and C.-K. Chou, “Post-processing errors in peak spatial-average SAR measurements of wireless handsets,” in *25th Annu. Bioelectromagnetics Society Meeting*, Wailea Maui, HI, June 2003, pp. 370–371.
- [11] N. Kuster and Q. Balzano, “Energy absorption mechanism by biological bodies in the near field of dipole antennas above 300 MHz,” *IEEE Trans. Veh. Technol.*, vol. 41, pp. 17–23, Feb. 1992.
- [12] Q. Yu, O. P. Gandhi, M. Aronsson, and D. Wu, “An automated SAR measurement system for compliance testing of personal wireless devices,” *IEEE Trans. Electromagn. Compat.*, vol. 41, pp. 234–245, Aug. 1999.
- [13] T. Schmid, O. Egger, and N. Kuster, “Automated E-field scanning system for dosimetric assessments,” *IEEE Trans. Microwave Theory Tech.*, vol. 44, pp. 105–113, Jan. 1996.
- [14] A. Drossos, V. Santomaa, and N. Kuster, “The dependence of electromagnetic energy absorption upon human head tissue composition in the frequency range 300–3000 MHz,” *IEEE Trans. Microwave Theory Tech.*, vol. 48, pp. 1988–1995, Nov. 2000.
- [15] “Additional Information for evaluating compliance of mobile and portable devices with FCC limits for human exposure to radiofrequency emissions,” FCC, Washington, DC, FCC OET Bull. 65, Supp. C, Ed. 01-01, June 2001.
- [16] M. Siegbahn and C. Törnevik, “A SAR test procedure for wireless devices with simultaneous multi-band transmission,” in *IEEE AP-S Int. Symp.*, vol. 2, June 2003, pp. 1033–1036.



**Michael Y. Kanda** (S'93–M'03) was born in Boulder, CO, on July 27, 1972. He received the B.S.E.E. degree from the University of Colorado at Boulder, in 1994, and the M.S.E.E. degree from the National Technological University, Minneapolis, MN, in 2003.

While at the University of Colorado at Boulder, he interned with Image Guided Technologies, Boulder, CO, where he was involved with calibration and accuracy evaluation of an optical three-dimensional (3-D) location system. In 1995, he joined Motorola Laboratories, Corporate Electromagnetic Energy (EME) Research Laboratory, Fort Lauderdale, FL, where he is the Deputy Technical Manager. His research has centered on RF dosimetry and dielectrometry. His current research focuses on techniques to improve RF product test accuracy and efficiency. He serves as a reviewer for several scientific journals.



**Mark G. Douglas** (S'86–M'98) received the B.Eng. degree from the University of Victoria, Victoria, BC, Canada in 1990, the M.Sc. degree from the University of Calgary, Calgary, AB, Canada in 1993, and the Ph.D. degree from the University of Victoria, in 1998, all in electrical engineering. His Master's thesis concerned the development of compact high-performance diversity antennas in wireless communications. His doctoral dissertation concerned the use and development of numerical modeling to study the electromagnetic interaction

between handheld wireless devices and the user.

From 1998 to 2002, he was a Senior Technical Leader with the Antenna Development Group, Ericsson Inc., Research Triangle Park, NC, where he was involved with antenna research and design for wireless handsets and managed an SAR compliance laboratory. He was also a member of the Ericsson EMF Research Group, Stockholm, Sweden, where he conducted research in RF dosimetry. In 2002, he joined the Corporate Electromagnetic Energy (EME) Research Laboratory, Motorola Laboratories, Plantation, FL, where he was a Distinguished Member of the Technical Staff. His research is in RF dosimetry. He has authored 20 refereed journal and conference papers. He holds five patents.

Dr. Douglas is a contributing member of the IEEE Standards Coordinating Committee 34, Subcommittee 2, and International Electrotechnical Committee, Project Team 62209, both concerning the development of SAR measurement standards. He is also a member of the Bioelectromagnetics Society.



**Edwin D. Mendivil** received the B.M.S. degree in signals and telecommunications from the Chorrillos Military Academy, Lima, Peru, in 1984, and the B.S. and M.S. degrees in electrical engineering from Florida Atlantic University, Boca Raton, in 1994 and 1996, respectively. His Master's thesis concerned the performance of ultrawide-band radars under clutter and stealth target environments.

In 1996, he joined the Corporate Electromagnetic Energy (EME) Research Laboratory, Motorola Laboratories, Fort Lauderdale, FL, where he has been involved in the development of software tools for the analysis and measurement of SAR.



**Maurice Ballen** was born in Cali, Colombia, in 1961. He received the A.S. degree in electronics from Broward Community College, Pompano Beach, FL, in 1984, and is currently working toward the B.S.E.E. degree at Florida Atlantic University, Boca Raton, FL.

Since 1984, he has been with Motorola. In 1993, he joined the Motorola Laboratories, Corporate Electromagnetic Energy (EME) Research Laboratory, Fort Lauderdale, FL. His research concerns the investigation of dielectrometry. He has contributed to several published papers, presentations, and standards.



**Andrew V. Gessner** was with the Department of Defense (DoD), U.S. Marine Corps from 1984 to 1988, where he was involved with testing, calibrating, and repairing military aircraft transponders and communication and navigation equipment. From 1990 to 1997, he was with the Allied Signal Corporation, Fort Lauderdale, FL, where he was involved in the test and development of traffic collision avoidance systems (TCAS) display indicators and transponders. Since 1998, he has been with the Corporate Electromagnetic Energy (EME) Research

Laboratory, Motorola Laboratories, Plantation, FL, where he has participated in EME test standards and EME compliance development.



**Chung-Kwang Chou** (S'72–M'75–F'89) received the B.S.E.E. degree from the National Taiwan University, Taipei, Taiwan, R.O.C., in 1968, the M.S. degree from Washington University, St. Louis, MO, in 1971, and the Ph.D. degree from the University of Washington, Seattle, in 1975, all in electrical engineering.

After spending a year as a National Institutes of Health Post-Doctoral Fellow with the Regional Primate Research Center and the Department of Physiology and Biophysics, University of Washington, he served as Assistant Professor from 1977 to 1981 and Research Associate Professor from 1981 to 1985 with the Department of Rehabilitation Medicine and Center for Bioengineering, University of Washington. From 1985 to 1998, he was a Research Scientist and the Director of the Department of Radiation Research, City of Hope National Medical Center, Duarte, CA. In April 1998, he joined Motorola Laboratories, Corporate Electromagnetic Energy (EME) Research Laboratory, Fort Lauderdale, FL. His current position is Chief EME Scientist, and the Director of the Corporate EME Research Laboratory, where he is responsible for RF product safety. His research has focused on RF biological effects, RF dosimetry and exposure systems, hyperthermia and electrochemical treatment of cancer. He was Associate Editor of the *Journal of Bioelectromagnetics* (1987–2003), for which he was responsible for editing papers on high-frequency RF fields.

Dr. Chou is a member of the Bioelectromagnetics Society, Tau Beta Pi, and Sigma Xi. He is a Fellow of the American Institute for Medical and Biological Engineering (1996). He has been chairman of the IEEE/Engineering in Medicine and Biology Society (EMBS) Committee on Man and Radiation (1996–1997) and co-chairman of the IEEE International Committee on Electromagnetic Safety Scientific Coordinating Committee 28, Subcommittee 4 on RF Safety Standard (1997–present). He was on the Board of Directors of the Bioelectromagnetics Society (1981–1984). He was vice chairman of Committee 89-5 of the National Council on Radiation Protection and Measurements (1996–1999), Council Member of the National Council on Radiation Protection and Medicine (NCRP) (1998–2004). He is the science adviser of the Mobile Manufacturers Forum (2001–present). He was the recipient of the first Special Award for the Decade (1970–1979) presented by the International Microwave Power Institute, the Outstanding Paper Award presented by the *Journal of Microwave Power* (1995), and the Curtis Carl Johnson Memorial Award for Preceptor of the Best Student Poster (1995) presented by the Bioelectromagnetics Society.